Earth and Planetary Science Letters 598 (2022) 117844

Contents lists available at ScienceDirect

Earth and Planetary Science Letters

www.elsevier.com/locate/epsl

Structure and dynamics of the Tonga subduction zone: New insight from P-wave anisotropic tomography

Zhiteng Yu [a,b,*], Dapeng Zhao [c], Jiabiao Li [a,**]

[a] Key Laboratory of Submarine Geosciences, Ministry of Natural Resources and Second Institute of Oceanography, Ministry of Natural Resources, 310012, Hangzhou, China
[b] Geo-Ocean, Univ Brest, CNRS, Ifremer, UMR6538, F-29280, Plouzané, France
[c] Department of Geophysics, Graduate School of Science, Tohoku University, 980–8578, Sendai, Japan

ARTICLE INFO

Article history:
Received 5 July 2022
Received in revised form 23 September 2022
Accepted 24 September 2022
Available online xxxx
Editor: H. Thybo

Keywords:
Tonga subduction zone
azimuthal anisotropy
Samoan plume
mantle flow
slab dehydration

ABSTRACT

The Tonga-Lau-Fiji region is important to study plate-plume and subduction-ridge interactions, but its deep mantle structure is still not very clear. Here we present high-resolution tomography of 3-D P-wave azimuthal anisotropy down to 400 km depth of the Tonga subduction zone derived from arrival-time data of local earthquakes recorded at seafloor and land seismometers. The subducting Tong slab is imaged as high-velocity anomalies at depths of 100-400 km, whereas large-scale low-velocity anomalies down to 400 km depth are revealed in the mantle wedge beneath the backarc basin and volcanic arc. Trench-parallel anisotropy beneath the Lau Basin extends southwards to ~140 km depth at ~20.5°S, representing the extent of both southward flow of the Samoan plume and toroidal flow by the slab rollback. At depths of 140-400 km, the Lau Basin and Fiji Plateau mainly exhibit plate-parallel fast-velocity directions (FVDs) north of ~20.5°S, indicating strong corner flow in the mantle wedge driven by the slab subduction and dehydration. The Tonga slab exhibits trench-parallel FVDs at depths of <200 km, reflecting fossil fabric formed during the plate spreading stage, whereas, at greater depths, the slab mainly exhibits trench-normal FVDs, which may reflect complicated deformations within the slab. These results suggest that the Samoan plume has a significant impact on the Tonga-Lau-Fiji region, leading to variations in the scale and depth extent of mantle flows.

1. Introduction

The Tonga-Lau-Fiji region in the southwest Pacific Ocean (Fig. 1) is a very complex trench-arc-backarc system, with features such as fast extension of the Lau backarc basin (Taylor et al., 1996), rapid plate convergence (Bevis et al., 1995), intense volcanic activity (e.g., the 2022 Tonga Hunga volcano eruption), and plate-plume (Samoa) interaction (Smith et al., 2001). A previous hypothesis suggests that variations in distance between spreading center and trench will cause variations in the Tonga subduction materials entering the Lau backarc basin (Martinez and Taylor, 2002), contributing to along-strike variations in the geological fingerprints, i.e., arc-like or mid-ocean ridge basalt (MORB)-like compositions (Escrig et al., 2009; Taylor and Martinez, 2003), and in axial morphology, i.e., axial high or axial valley (Martinez et al., 2006). Recent geophysical studies further indicate that the supply of the Australian mantle materials in the west also influences spreading processes in the Lau Basin (Wei et al., 2016). Previous studies of seismic anisotropy (Chang et al., 2016; Menke et al., 2015; Smith et al., 2001; Wei et al., 2016; Zha et al., 2014) and geochemistry (Pearce et al., 2007; Turner and Hawkesworth, 1998) have proposed that the northern Samoan mantle plume flows into the Lau Basin through a tear of the Pacific plate (Millen and Hamburger, 1998), affecting the backarc extension and arc volcanism, however, the flow depth extent is still unclear. In addition, Samoan-plume materials have been traced along the Vitiaz Lineament to the northwest Fiji Plateau (Price et al., 2014), having a long-run impact on the mantle flow beneath the Lau Basin in the last 4 Myr (Hart et al., 2004; Price et al., 2014). A recent seismic study also revealed a depressed 410-km discontinuity around the Fiji Plateau, which is attributed to the hot Samoan-plume material (Li et al., 2019).

All these above-mentioned features demonstrate the complexity of mantle dynamics of the Tonga subduction zone, and high-resolution seismic imaging can provide direct evidence and constraints on these processes. There have been several models of two-dimensional and three-dimensional (3-D) seismic tomography

* Corresponding author at: Key Laboratory of Submarine Geosciences, Ministry of Natural Resources and Second Institute of Oceanography, Ministry of Natural Resources, 310012, Hangzhou, China.
** Corresponding author.
E-mail addresses: ztyu@sio.org.cn (Z. Yu), jbli@sio.org.cn (J. Li).

https://doi.org/10.1016/j.epsl.2022.117844

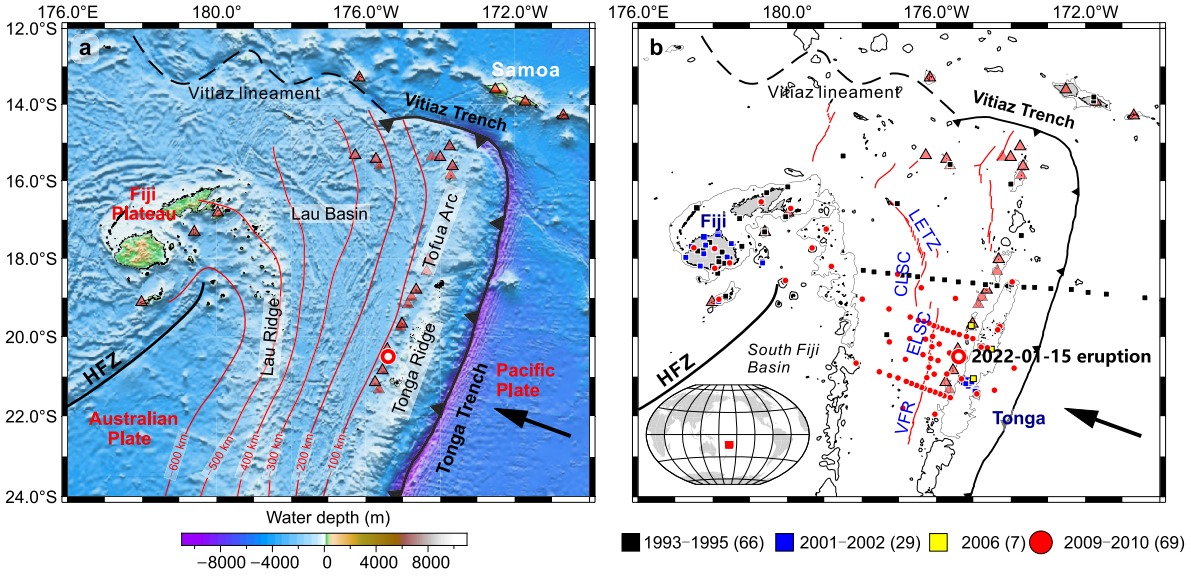

Fig. 1. Maps of the study area. (**a**) Bathymetry of the study area. Red lines show the depth contours of the Tonga slab upper boundary from the Slab2 model (Hayes et al., 2018) for reference. The black jagged line denotes the Tonga Trench. Red triangles indicate active volcanoes. The red and white concentric circle marks the location of the Hunga Tonga–Hunga Ha'apai eruption on 15 January 2022. (**b**) Seismic experiments and main tectonic features. Red lines indicate the backarc spreading centers modified from Conder and Wiens (2006). Seismic stations used in this study from four seismic experiments are shown in black squares (1993-1995), blue squares (2001-2002), yellow squares (2006), and red dots (2009-2010). The inset map shows location of the study region (red square). The other labeling is the same as that in (**a**). HFZ = Hunter fracture zone; LETZ = Lau extensional transform zone; CLSC = Central Lau Spreading Center; ELSC = Eastern Lau Spreading Center; VFR = Valu Fa Ridge. (For interpretation of the colors in the figure(s), the reader is referred to the web version of this article.)

of the Tonga-Lau-Fiji region obtained by different methods and from several seismic experiments (Conder and Wiens, 2006; Roth et al., 1999; Wei et al., 2016, 2015; Wei and Wiens, 2018; Zha et al., 2014; Zhao et al., 1997), however, either their low resolutions (>50 km) or their shallow depth ranges (<200 km depth) restrict our understanding of the deep structure beneath the whole area. A detailed 3-D model of depth-varying anisotropy is needed to investigate the 3-D mantle flow field at depth. In this study, we determine the first 3-D model of P-wave velocity (Vp) azimuthal anisotropy from the Tonga trench to the Fiji Plateau, using a large number of P-wave arrive times of local earthquakes recorded at seafloor and land seismic stations from four seismic experiments during 1993-2010 (Fig. 1b). Our model presents a detailed structure of mantle flow beneath the backarc spreading center and volcanic arcs, providing new insights into mantle dynamics associated with a mantle plume in a cold subduction zone.

2. Tectonic settings

The Tonga subduction zone is located in the southwest Pacific Ocean, where the Pacific plate subducts beneath the Indo-Australian Plate, with a fast convergence rate of up to 240 mm/yr (Bevis et al., 1995) (Fig. 1a). The Lau Basin is an active backarc basin behind the Tonga arc and is bounded by a remnant island arc (Lau Ridge) on the west and a still-active volcanic arc (Tofua Arc) and the extinct Tonga Ridge on the east (Fig. 1a). To the northern end, it is bounded by the Vitiaz Lineament (Fig. 1a), which marks the traces of the paleo-subduction of the Pacific-Australian convergence until ~12 Ma (Hawkins, 1995), and represents the location of possible tearing of the Pacific plate (Millen and Hamburger, 1998). To the northeast of the Tonga Trench, there is an oceanic hotspot—Samoa (Fig. 1), which can be recognized by an age-progressive volcanic chain on the seafloor (Hart et al., 2004) (Fig. 1) and is thought to be a deeply rooted mantle plume (Jackson et al., 2010), and its lavas contain some recycled subducted continental crust materials (Jackson et al., 2007).

The V-shaped Lau Basin is ~450 km wide in the north (15°S) and ~200 km wide in the south (25°S) (Keller et al., 2008), indicating southward decreasing distances to the Tonga Trench (Fig. 1). The Lau Basin has been opening in the last ~6 Myr (Taylor et al., 1996), with several mature seafloor-spreading centers propagating southwards. From north to south, the spreading system includes three major centers by the axial morphology (Martinez et al., 2006): the Central Lau Spreading Center (CLSC, ~18°–19°20′S), the Eastern Lau Spreading Center (ELSC, 19°20′–21°26′S), and the Valu Fa Ridge (VFR, 21°26′–22°45′S), see Fig. 1b. The spreading rates decrease southwards from 95 to 35 mm/yr (Martinez et al., 2006). Due to the increasing influence of subduction with decreasing distance from spreading center to trench from north to south (Martinez and Taylor, 2002; Taylor et al., 1996), there seems to be a transition zone at the latitude of ~20.6°S not only for axial morphology (Martinez et al., 2006) but also for the crustal composition (Escrig et al., 2009). To the south, the axial axis is marked by an axial high (Martinez et al., 2006), showing arc-like composition basalts with low Mg contents (Escrig et al., 2009). In contrast, to the north, the axial axis is characterized by an axial valley (Martinez et al., 2006), with MORB-like basaltic compositions (Escrig et al., 2009).

3. Data and methods

3.1. Data collection

In this work, we collected arrival-time data of local earthquakes recorded at ocean-bottom seismometers (OBSs) and land seismic stations deployed in the Tonga-Lau-Fiji region during four seismic experiments in 1993-1994, 2001-2002, 2006, and 2009-2010 (Fig. 1b). A total of 171 seismic stations are used in this work (Table S1). We picked P- and S-phases manually on seismograms of 1029 events ($M \geq 4.0$) during 2001-2010, which were acquired from the IRIS data center (https://ds.iris.edu/ds/nodes/dmc/). We also used the arrival-time data of 926 local earthquakes recorded during 1993-1995 in the study region (Zhao et al., 1997). As a result, our data set includes 23,781 P-arrivals and 5878 S-arrivals from a total of 1955 local earthquakes (Table S1).

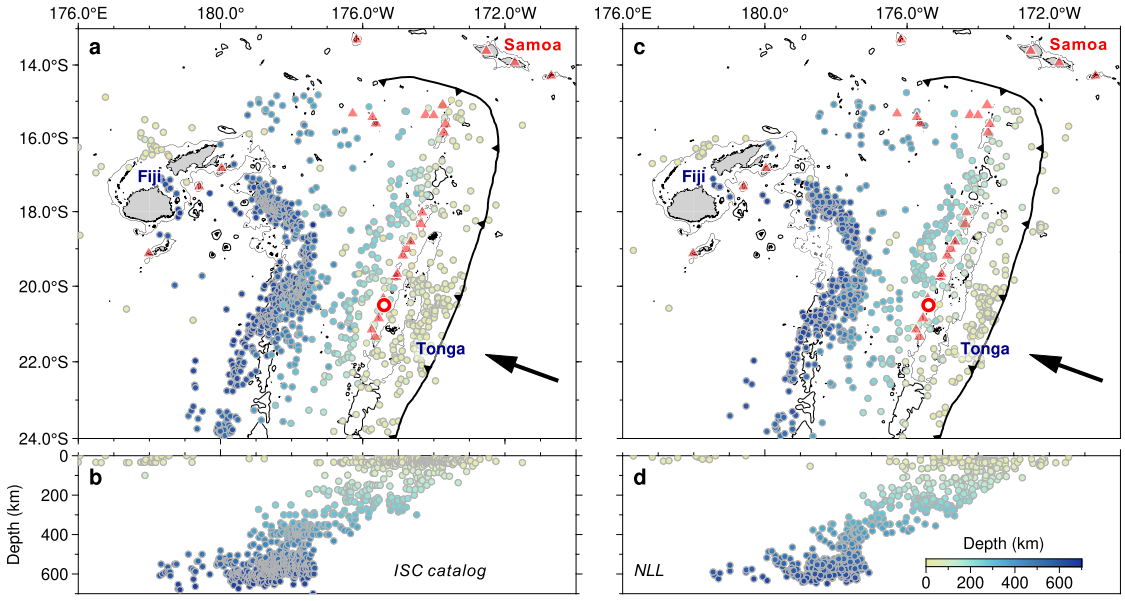

Fig. 2. Earthquakes used in the tomographic inversion. (**a**) Original catalog epicenters from the International Seismological Center (ISC). Land areas and water areas with depths of <1 km are shaded in gray and marked by black lines respectively. (**b**) East-west vertical cross-section of the events in (**a**). (**c**) Epicentral distribution of the earthquakes relocated using the NonLinLoc program (Lomax et al., 2000). (**d**) East-west vertical cross-section of the events in (**c**). The colors of dots denote focal depths, whose scale is shown in (**d**). The other labeling is the same as that in Fig. 1.

Table 1
Details of the dataset used for the tomographic inversion. Note that the S-wave arrivals are insufficient to conduct a tomographic inversion.

Period	Number of seismic stations	Number of earthquakes	Number of P-arrivals	Number of S-arrivals
1993-1995	66	255	2551	1188
2001-2002	29	144	1697	168
2006	7	54	328	542
2009-2010	69	413	7783	727
Total	171	866	12,359	2625

These earthquakes are then relocated by using a nonlinear oct-tree search algorithm of the NonLinLoc program (Lomax et al., 2000) and the IASP91 one-dimensional (1-D) Vp model (Kennett and Engdahl, 1991). To improve the hypocentral parameters, we also included arrival-time data recorded at global seismic stations, which were selected from the Bulletin of the International Seismological Center (ISC) (http://www.isc.ac.uk) (Fig. 2a-2b), with epicentral distances up to 95° (Fig. S1) for each event. The ISC travel-time data are only used for relocating the earthquakes. We chose the maximum likelihood location as the preferred solution for each event. Iterative calculations of station corrections were performed to find the best solution as well as to remove the 3-D structural effects when the average root mean square (RMS) misfit yields a minimum (Fig. S2). To conduct the tomographic inversion, we selected the relocated earthquakes with RMS residual times of <1 s, epicentral uncertainties of <20 km, and depth uncertainties of <15 km (Fig. S3). As a result, 12,359 P-wave arrivals of 866 events are used for the Vp tomographic inversion (Fig. 2c-2d, Table 1). Due to the poor quality of waveforms, we could not pick a sufficient number of S-wave phases (Tables 1 and S1) to perform S-wave travel-time tomography, nor could we perform waveform tomography in this study. Our 3-D P-wave isotropic and anisotropic models would provide a good starting model for performing full waveform inversions in the future.

3.2. Vp anisotropic tomography

We used a tomographic method (Zhao et al., 2012, 1992) to study the regional 3-D isotropic Vp structure beneath the study region. To express the 3-D velocity structure, we set up a 3-D grid in the modeling space at longitudes 176°E -170°W and latitudes 24°S-14°S. In this study, the subducting Tonga slab is not included in the starting model due to the large uncertainty of the slab upper boundary and slab thickness (Hayes et al., 2018). Lateral depth variations of the Conrad and Moho discontinuities from the CRUST 1.0 model (Laske et al., 2013) are included in the starting model for the tomographic inversion. Isotropic Vp perturbations at the grid nodes from a starting 1-D model (the IASP91 model) (Kennett and Engdahl, 1991), are taken as unknown parameters. The isotropic Vp perturbation at any point is calculated by linearly interpolating the isotropic Vp perturbations at the eight grid nodes surrounding that point (Zhao et al., 2012, 1992). We used an efficient 3-D ray-tracing technique (Zhao et al., 1992) to calculate theoretical travel times and ray paths accurately. Station elevations and surface topography are taken into account in the 3-D ray tracing. The LSQR algorithm (Paige and Saunders, 1982) is used to solve the large but spare system of observation equations.

The 3-D azimuthal anisotropy and isotropic Vp variation are simultaneously determined by using the method of Liu and Zhao (2016) based on the assumption of weak orthorhombic anisotropy with a horizontal symmetry plane. P-wave anisotropic slowness can be expressed as:

$$S = S_0 + M\cos 2\theta \tag{1}$$

where S is the total P-wave slowness, S_0 is the average azimuthal P-wave slowness (i.e., the isotropic component), M is a parameter for anisotropy, and θ is the angle between the ray propagation direction and the symmetry axis. The P-wave slowness can be approximately expressed as:

$$S(\emptyset) = S_0[1 + A\cos 2\emptyset + B\sin 2\emptyset] \tag{2}$$

where A and B are two parameters for azimuthal anisotropy, and $\emptyset$ is the ray path azimuth. The fast-velocity direction (FVD) Ψ and the amplitude (α) of azimuthal anisotropy can be expressed as:

$$\Psi = \left\{ \begin{array}{l} \frac{1}{2}\tan^{-1}\frac{B}{A} + \left\{ \begin{array}{ll} \frac{\pi}{2}, & A > 0 \\ 0, & A < 0 \end{array} \right. \\ -\frac{\pi}{4}, \quad A = 0,\ B > 0 \\ \frac{\pi}{4}, \quad A = 0,\ B < 0 \end{array} \right\} \tag{3}$$

$$\alpha = \frac{\sqrt{A^2 + B^2}}{1 - \left(A^2 + B^2\right)} \tag{4}$$

To determine a 3-D anisotropic Vp model, a fine 3-D grid is arranged in the study volume to express the isotropic Vp structure, and a coarse 3-D grid is arranged to express azimuthal anisotropy parameters (A and B), which are unknown parameters to be determined by a tomographic inversion. Both the parameters A and B are zero in the starting model. The grid interval for the anisotropic grid (0.50°) is larger than that for the isotropic grid (0.33°) (Fig. 3) because better ray crisscrossing is required to resolve 3-D Vp anisotropy. The grid meshes are set at depths of 10, 25, 40, 65, 90, 115, 140, 180, 230, 280, 330, 380, 430, 480, 530, 580, 630, and 700 km in the study volume. The anisotropic Vp perturbation at any point is calculated by linearly interpolating its perturbations at the eight grid nodes surrounding that point (Liu and Zhao, 2016). Similar to the isotropic inversion, we used the LSQR algorithm (Paige and Saunders, 1982) to determine the 3-D A and B parameters. After the inversion, we used the resulting A and B to obtain the FVD and amplitude of Vp azimuthal anisotropy at any point using the equations (3) and (4).

We conducted many tomographic inversions with different damping and smoothing parameters to draw tradeoff curves between the root-mean-square (RMS) travel-time residual and the norm of the 3-D Vp model (Fig. S4). The optimal damping and smoothing parameters are found to be 3.0 and 2000.0, respectively, from the tradeoff curves. In the inversion, the hypocentral parameters determined by the NonLinLoc program are fixed. The optimal 3-D Vp anisotropic model is obtained after eight iterations (Fig. S5). The different RMS residuals in Figs. S4 and S5 are due to the absence of smoothing regularization in Fig. S4. Only the data with travel-time residuals <2 s are used in the inversion (Fig. S6). After the isotropic and anisotropic inversions (Fig. S4), the RMS travel-time residual is reduced to 0.46 s and 0.36 s, respectively, indicating that the anisotropic tomography could reduce the RMS residual substantially by ~22%.

3.3. Resolution tests

We performed extensive checkerboard resolution tests (CRTs) (Zhao et al., 1992) to assess the reliability of the obtained tomographic model (Figs. S7-S17, Table S2). To make a checkerboard model, ±3% perturbations to the isotropic Vp parameters and ±3% perturbations to the anisotropic parameters (A and B) are assigned alternately to the 3-D grid nodes. The ±3% perturbations of A and B result in an azimuthal anisotropy with an amplitude of 4.25% and an FVD of 112.5° or 22.5°. Then theoretical travel times for the synthetic checkerboard model are calculated, which are then inverted to obtain an output model (the recovered model). Finally, we investigated whether the input checkerboard model could be recovered or not. To simulate the picking errors of the arrival-time data, we added random noise (−0.2 to +0.2 s) with a standard deviation of 0.1 s to the synthetic travel times before conducting the inversion.

We performed the first set of CRTs for the isotropic Vp tomography with different lateral grid intervals of 0.25°, 0.33°, and 0.5° (Figs. S7-S9), in which the Vp anisotropy was not inverted. The second set of CRTs is for the Vp anisotropy with lateral grid intervals of 0.33° (Fig. S10), 0.5° (Fig. 3), and 0.66° (Fig. S11). The test results show that the lateral resolution is ~0.33° for the isotropic Vp model and ~0.5° for the Vp azimuthal anisotropy (Fig. 3). Both the isotropic and anisotropic structures of the Tonga-Lau-Fiji region can be well resolved, except for the area between the Lau Ridge and the Fiji Plateau at shallow depths (<140 km) due to the poor ray path coverage there (Fig. 3, Figs. S7-S11).

To investigate the possible trade-off between the obtained isotropic and anisotropic components, we performed the third set of CRTs with ±3% anomalies of Vp anisotropy but without isotropic Vp anomalies (Figs. S12-S14). In the fourth set of CRTs, the input model contains ±3% isotropic Vp anomalies but has no anisotropic anomalies (Fig. S15-S17). The test results show that the trade-off between the Vp isotropy and anisotropy is insignificant in most parts of the study volume (Figs. S12-S17). Strong trade-off occurs beneath the Fiji Plateau at depths of <200 km, where the ray paths do not crisscross very well (Figs. S12-S17).

To evaluate the robustness of main features of the obtained isotropic Vp image and azimuthal anisotropy, we also performed several restoring resolution tests (RRTs) (Figs. S18-25, Table S2). The procedure of the first RRT (Figs. S18 and S19) is similar to that of the CRT but the input model is derived from the obtained 3-D Vp model (Figs. 4 and 5) instead of a checkerboard model. The other two RRTs were performed to further examine the trade-off effect (Figs. S20-S23). In addition, we conducted the fourth RRT with FVD orientations in the input model perpendicular to the obtained FVDs, in order to evaluate the influence of the initial model (Figs. S24 and S25). These RTTs and trade-off tests show that the main features of our tomographic images can be well recovered, and the trade-off is not obvious, indicating that our tomographic results are quite robust.

4. Results

4.1. Isotropic Vp tomography

Large-scale low-velocity (low-V) anomalies (Figs. 4 and 5) are clearly revealed beneath the spreading center of the Lau Basin and volcanic arc in the mantle wedge. The low-V anomalies extend to ~400 km depth (Figs. 4 and 5), which is similar to the previous tomographic result (Zhao et al., 1997). This low-V zone is slightly broader beneath the CLSC and ELSC (200-400 km wide) than that beneath the VFR (~150 km wide) (Figs. 4 and 5). In addition, the broader anomalies are mainly located at depths of <200 km north of ~20°S (Figs. 4 and 5). Our tomographic results do not show a discernible pattern between the Tonga arc (Tonga Ridge and Tofua Arc) and the Lau Basin at shallow depths as suggested before (Zhao et al., 1997), which are connected instead (Figs. 4 and 5).

The subducting Tonga slab is revealed as high-velocity (high-V) anomalies at depths of ~100-400 km but is not well solved at shallow depths (Figs. 4 and 5) due to the limited ray coverage in the northern Lau Basin where shallow- and intermediate-depth earthquakes are not well determined in this study (Fig. 2). In addition, our tomographic model cannot reveal the high-V anomalies at depths of >400 km (Fig. 5) due to the limited rays passing through the subducting slab in that depth range (Fig. 2).

4.2. Vp anisotropic tomography

Beneath the CLSC and ELSC of the Lau Basin, trench-parallel (nearly N-S) FVDs are well revealed at depths of <140 km (**A1** in Figs. 4 and 5). Our anisotropic tomography has lower resolution at the shallow part (< 40 km depth), so the expected W-E FVDs related to the backarc seafloor spreading are not observed (Figs. 4 and 5). At depths of >140 km, FVDs change to NW40-60° (**A2** in Figs. 4 and 5), parallel to the subducting direction of the Pacific plate. Beneath the VFR (south of ~21°S), some trench-parallel FVDs are revealed (**A3** in Figs. 4 and 5). There seems to be a boundary that separates the NW FVDs in the CLSC and ELSC and

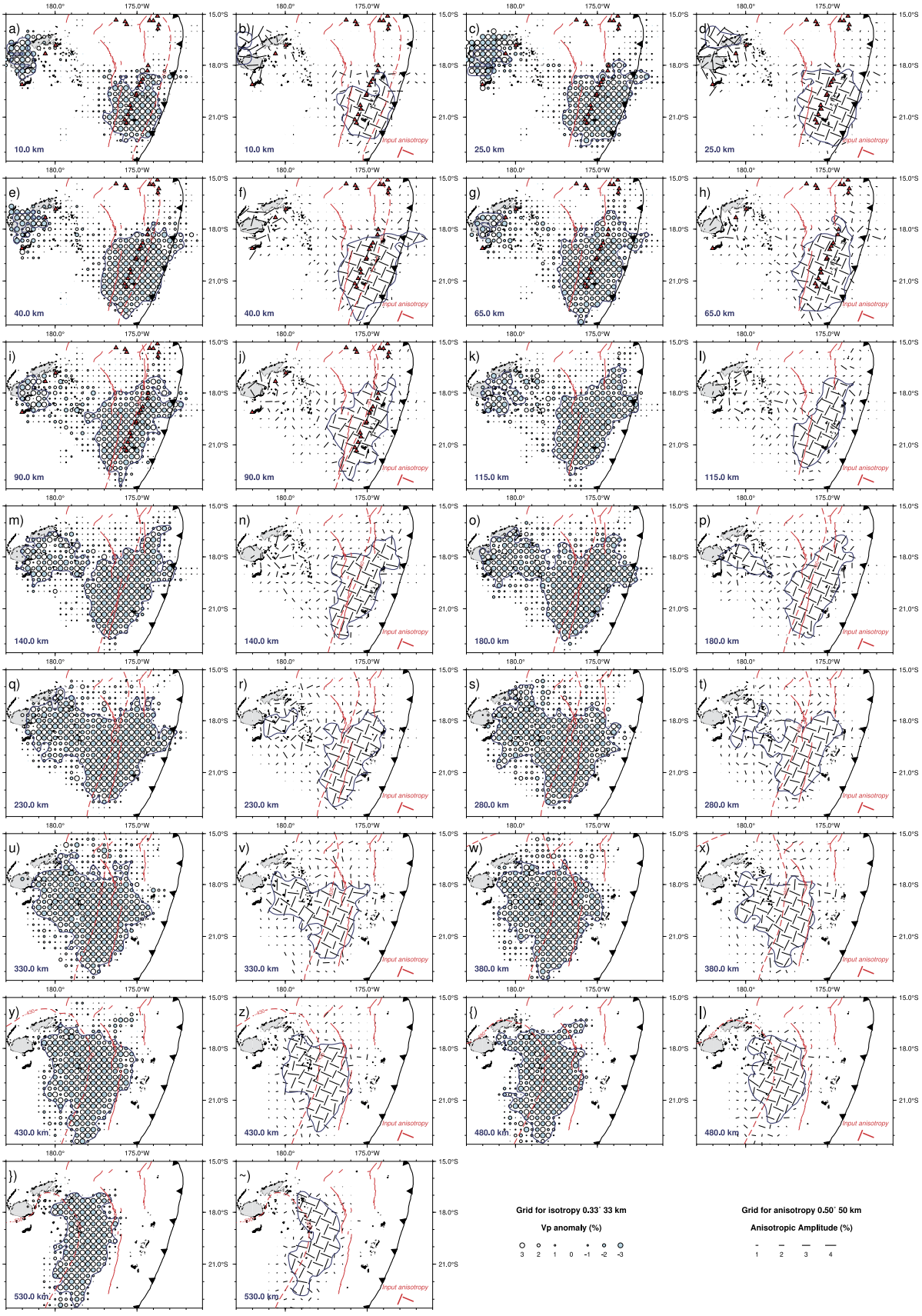

Fig. 3. The checkerboard resolution test for Vp azimuthal anisotropic tomography. The lateral grid intervals are 0.33° and 0.50° for the Vp isotropic and anisotropic anomalies, respectively. The dashed red lines show the upper boundary of the subducting Tonga slab from the Slab2 model (Hayes et al., 2018) for reference. The input amplitudes of Vp perturbations are ±3%, whose scale is shown at the bottom-right. The black bars represent Vp azimuthal anisotropy, whose orientation and length denote the FVDs and the amplitude of anisotropy, respectively. The red bars on each map show the input Vp anisotropy for reference. The dark blue line on each map indicates the regions with a restored amplitude greater than 50%, which is used in Figs. 4 and 5.

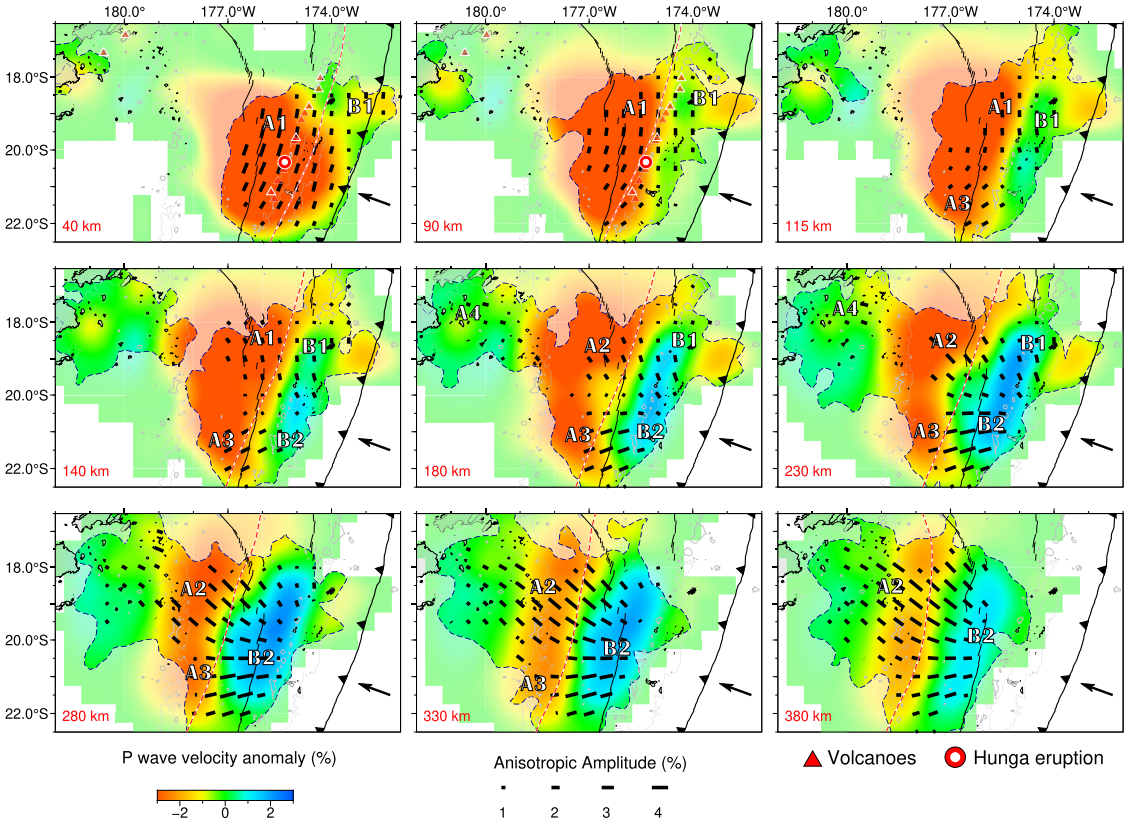

Fig. 4. Map views of Vp azimuthal anisotropic tomography at nine depths. The layer depth is marked at the lower-left corner of each map. The background colors indicate isotropic Vp perturbations, whose scale is shown at the bottom. The dashed blue lines outline the well-resolved parts. The orientation and length of the short black bars represent the FVD and the anisotropic amplitude, respectively, which are well restored by the resolution test in Fig. 3. The anisotropic amplitude scale is shown at the bottom. The main Vp anisotropic features in the mantle wedge (**A1**-**A4**) and within the slab (**B1**-**B2**) are marked (see the main text). The other labeling is the same as that in Fig. 3.

NE to W-E FVDs in the VFR at ~20.5°S (**A3** in Figs. 4 and 5). Beneath the Fiji Plateau and Lau Ridge, nearly W-E FVDs are revealed at depths of 140-230 km (**A4** in Fig. 4) and NW FVDs at greater depths (**A4** in Figs. 4 and 5).

In the subducting Pacific slab, FVDs in the north of ~20.5°S are roughly trench-parallel at depths of <200 km (**B1** in Figs. 4 and 5) but are trench-normal at depths of >200 km (**B2** in Figs. 4 and 5). In contrast, FVDs in the south of ~20.5°S are mostly trench-normal (W-E) at depths of >140 km (**B2** in Figs. 4 and 5).

5. Discussion

5.1. Mantle flow beneath the Lau Basin

5.1.1. Effect of the Samoan plume

Our anisotropic tomography provides new depth constraints on mantle flow and dynamics beneath the Lau Basin. The broad low-V anomalies in the mantle wedge are consistent with previous tomographic results (Conder and Wiens, 2006; Wei et al., 2016, 2015; Zha et al., 2014; Zhao et al., 1997), where high P-wave attenuation was also observed (Roth et al., 1999; Wei and Wiens, 2018). These features indicate a hot and strong mantle flow in the mantle wedge. The observed trench-parallel FVDs (nearly N-S) beneath the Lau Basin (**A1**, Figs. 4 and 5) are consistent with previous S-wave splitting and ambient-noise tomographic results (Chang et al., 2016; Menke et al., 2015; Smith et al., 2001; Wei et al., 2016), which have been interpreted as the Samoan plume flowing into the Lau basin through the northern slab tear (Smith et al., 2001; Turner and Hawkesworth, 1998) (Fig. 6). Geochemical studies showed high $^{3}He/^{4}He$ ratios in the northern part of the Lau Basin, indicating the input of the Samoan-plume material (Lupton et al., 2009; Turner and Hawkesworth, 1998). Our observed depth-varying FVDs suggest that the plume related flow extends southwards to ~140 km depth and to ~20.5°S at most (Figs. 4–6), and have a strong impact on the CLSC and ELSC. In contrast, the southern VFR exhibits substantial NE-SW to W-E FVDs instead of N-S FVDs at most depth layers (**A3** in Figs. 4 and 5), suggestive of much weaker effects of the Samoan plume. This southward N-S flow may be driven by the strong slab rollback in the Tonga subduction zone, which is supported by numerical simulation results (Alisic et al., 2012). In addition, our results suggest that the slab rollback could also introduce a toroidal flow (Foley and Long, 2011; Schellart and Moresi, 2013), contributing to the backarc extension beneath the CLSC and ELSC (Fig. 6).

In this study, our observed trench-parallel FVDs are not perfectly aligned as previously suggested (Menke et al., 2015; Wei et al., 2016), which are oriented nearly N-S, ~25° to the Tonga Trench orientation (**A1** in Fig. 4). We found a clear westward shifting trend of FVDs with the increasing depths beneath the CLSC and ELSC (north of 21°S) (Fig. 4), which may indicate the influence of deep corner flow in the mantle wedge (NW-SE FVDs, **A2** in Fig. 4). Therefore, we suggest that this shifting of FVDs reflects the combined effects of the plate-parallel mantle wedge flow in the deep part and trench-parallel flow at depths of <140 km (Wei et al., 2016).

5.1.2. Deep corner flow in the mantle wedge

NW-SE trench-normal anisotropy (**A2** in Figs. 4 and 5) occurs at depths of >140 km in the mantle wedge beneath the Lau Basin north of ~20.5°S, which may reflect lattice preferred orientation (LPO) of olivine crystals caused by shear strain due to the slab-driven corner flow (Karato et al., 2008) (Fig. 6), as observed in other subduction zones, e.g., Tohoku (Liu and Zhao, 2017; Zhao

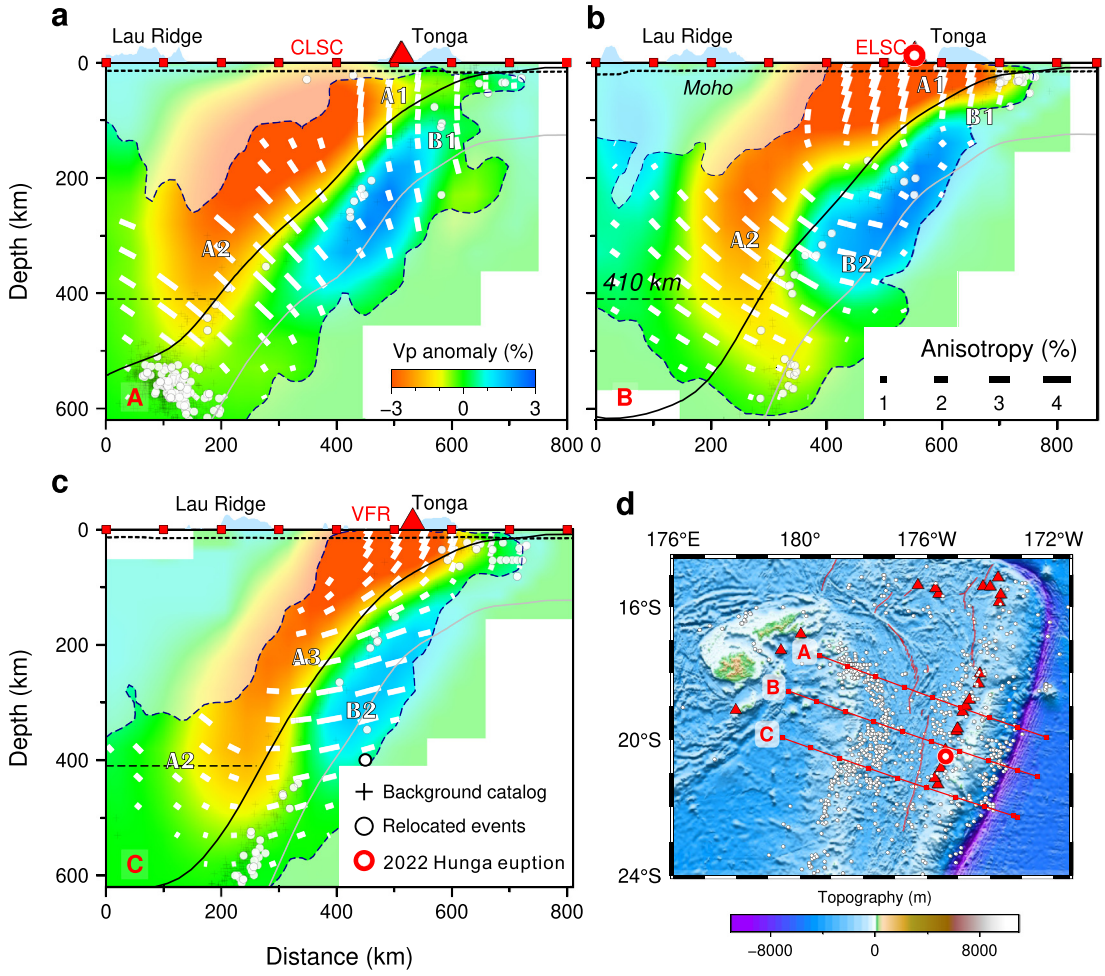

Fig. 5. Three vertical cross-sections of Vp azimuthal anisotropic tomography (**a**-**c**). Their locations are shown in (**d**). Azimuthal anisotropy is marked in white bars, i.e., the vertical bars denote north-south FVDs, whereas the horizontal bars denote east-west FVDs. Land areas (light blue patches) and 100-km intervals (red squares) are shown on the top for inference. The black crosses denote the background seismicity from the ISC bulletins, while white dots are the events used for the tomographic inversion (Fig. 2c-2d). The dashed black lines mark the Moho and 410-km discontinuities. The black line denotes the upper boundary of the subducting Tonga slab. The other labeling is the same as that in Fig. 4.

et al., 2016). These trench-normal FVDs are also observed beneath the Fiji Plateau and Lau Ridge by other anisotropic studies (Fischer et al., 2000; Smith et al., 2001), indicating that the strong corner flow in the mantle wedge is driven by the slab subduction and dehydration (Fig. 6).

In the south of ~20.5°S, FVDs rotate between NE-SW and nearly W-E at depths of 100-300 km (**A3** in Figs. 4 and 5). Similar FVD patterns have been observed beneath the Lau Ridge and Fiji Plateau by Wei et al. (2016), which are interpreted as LPO by slab-driven counter flow (Karato et al., 2008) (**A4** in Fig. 4). Previous geochemical studies have observed abrupt variations in crustal composition and axial morphology from the northern ELSC to the southern VFR at ~20.5°S (Escrig et al., 2009) and suggested that they are due to the increasing subduction material input, which is resulted from the decreasing distance between spreading centers and the Tonga slab from north to south (Dunn and Martinez, 2011; Martinez and Taylor, 2002; Taylor et al., 1996). Rayleigh-wave tomographic results (Wei et al., 2016) show that this transition is also related to the influence of the western incoming Australian mantle, which enters the northern Lau Basin (CLSC and ELSC) but does not enter the southern VFR, leading to different geochemical compositions from north to south (Wei et al., 2016). Our present tomography cannot resolve the structure in the west of the Lau Ridge, so it cannot provide constraints on the presence of the Australian upwelling flow. Our results show that the low-V zones beneath the northern ELSC and CLSC and the Tofua arc are broader than that beneath the southern VFR (Fig. 4). The southern VFR is more influenced by the Tonga subduction processes than the Samoan plume (Martinez and Taylor, 2002; Taylor and Martinez, 2003). We suggest that the NW-SE to W-E FVD patterns beneath the VFR may indicate a strong counterflow at shallow depths (~100-300 km), reflecting stronger effects of the subduction processes in this area in comparison to the CLSC and ELSC.

We conclude that the influence of the Samoan plume in-flow and the toroidal flow extend down to ~140 km depth beneath the Lau backarc spreading center and Tofua Arc, whereas the wedge corner flow prefers to occur in a deeper mantle (~140-400 km depths) on the western flank (Fig. 6), which also contributes to the magmatism beneath the spreading center and volcanic arc.

5.2. Mantle flow beneath the Fiji Plateau

A recent seismic study (Li et al., 2019) shows that the 410-km discontinuity is depressed close to the northwestern Fiji Plateau, implying possible migration of the Samoan plume from the hot spot to the west (Fig. 6). Geochemical studies (Hart et al., 2004; Price et al., 2014) also suggest that the Samoan plume may extend to a broad area from east to west, as far as the North Fiji Basin. As a result, due to the strong rollback of the Tonga slab (Alisic et al., 2012), the Samoan-plume material would be expected to flow into

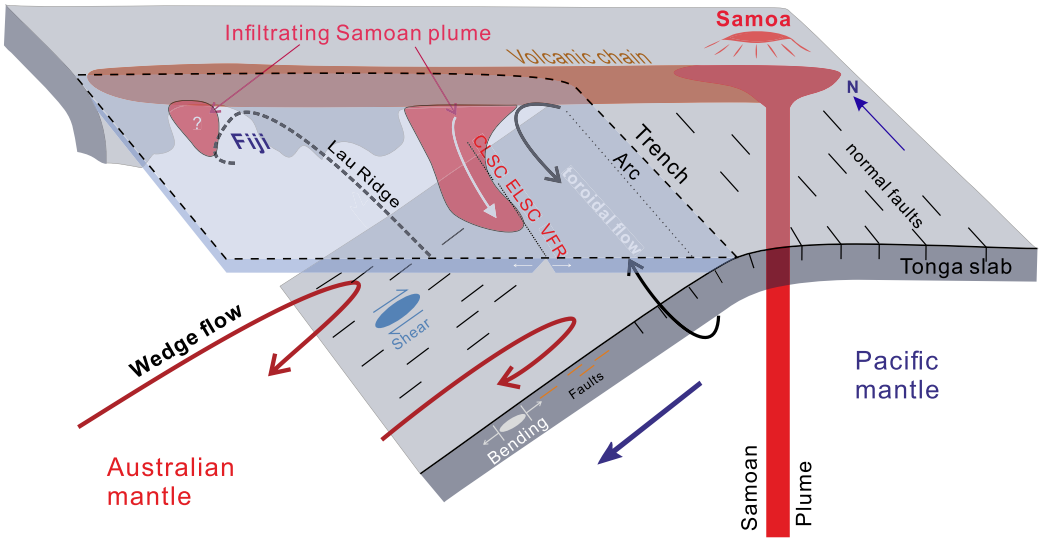

Fig. 6. A schematic diagram showing mantle dynamics of the Tonga subduction zone. This cartoon is modified from previous studies (Price et al., 2014; Turner and Hawkesworth, 1998). The blue shade indicates simplified tectonic information on the seafloor.

the Fiji Plateau, which would lead to the presence of low-V anomalies and N-S FVDs beneath the Fiji Plateau as those beneath the Lau Basin at depths of <140 km. However, the expected large-scale low-V zone is not revealed in our result (Fig. 4). In addition, our observed FVDs rotate from W-E to NW40-60° at depths of ~200-400 km, indicating a strong corner flow in the mantle wedge (**A4** in Fig. 4). That is to say, even if the plume has been persistent in the northwestern Fiji Plateau in the past 4 Myr (Hart et al., 2004; Price et al., 2014), it would have been localized in its starting area, without obvious southward "tongues" of Samoan-plume material (Price et al., 2014) flowing into the Fiji Plateau and the east Lau Ridge (Fig. 6). In other words, most infiltrating Samoan-plume materials have been flowing into the Lau basin at shallow depths of <140 km through a slab tear close to the Tonga Trench (Price et al., 2014) before migrating to the west (Fig. 6).

5.3. Anisotropy in the Tonga slab

The subducting Tonga slab at depths of ~100-400 km is well revealed as a high-V anomaly but cannot be resolved at other depths due to the limited ray coverage (Figs. 3–5). The trench-parallel FVDs in the slab are mainly observed at depths of <200 km (**B1** in Figs. 4 and 5), which have been widely found in other subducting slabs. The slab anisotropy is commonly explained as fossil fabric, which was generated during the spreading stage at a mid-ocean ridge (e.g., Liu and Zhao, 2017; Wang and Zhao, 2008) (Fig. 6). Note that an ancient spreading center, the Osbourn Trough, is currently subducting at the Tonga Trench (Worthington et al., 2006), whose strike is normal to the Tonga Trench, corresponding to trench-normal FVDs. However, the Osbourn Trough is located at ~25.5°S, and only ~150 km wide (Worthington et al., 2006), which extends northward to 25°S, beyond our study region. It is also possible that these trench-parallel FVDs in the slab at shallow depths are related to the hydrated normal faults (Fig. 6), which are due to the along-strike horizontal extension at the out-rise region as shown in the Mariana Trench (Wang et al., 2022; Wang and Zhao, 2021; Zhou et al., 2015).

At 230-430 km depths, trench-normal FVDs are widely observed within the slab south of ~20.5°S (**B2** in Figs. 4 and 5), which are likely associated with the present deformation in the slab (Eakin et al., 2016). Bonnardot et al. (2009) suggested that there is a stress state transition at ~21°S in the Tonga slab, i.e., a double stress regime (downdip compression in the upper plane and downdip extension in the lower plane of the double seismic zone) is observed in the north of ~21°S, whereas only downdip compression is revealed in the south of ~21°S. Therefore, we suggest that this stress state transition may lead to the slab bending, producing the trench-normal extension in the south of 20.5°S (Fig. 6), as observed in the northern Chile subduction zone (Huang et al., 2019). However, this hypothesis needs further evidence from other multidisciplinary studies. Another possibility is that the FVDs are produced by the subduction-related shearing strains or faulting (Fig. 6) when the slab sinks into the deeper mantle, as revealed in the Tohoku subduction zone (Liu and Zhao, 2017).

6. Conclusions

To investigate the deep mantle structure and flows of the Tonga-Lau-Fiji region, we determine a high-resolution 3-D model of Vp anisotropic tomography of the Tonga subduction zone using a large number of P-wave arrival times of relocated local earthquakes recorded at the seafloor and land seismometers from the past four seismic experiments. Our results provide new insights into mantle dynamics beneath the Tonga region. The Tonga slab is revealed as high-V anomalies at depths of ~100-400 km, and the mantle wedge beneath the Lau Basin and Tofua Arc exhibits large-scale low-V anomalies, indicating hot and wet mantle upwelling. Trench-parallel FVDs are observed at depths of <140 km beneath the Lau Basin, indicating that the Samoan plume from the north slab tear flowing into the basin and toroidal flow by the slab rollback extend to ~140 km depth in the mantle wedge. In addition, the Samoan plume flow may stop at ~20.5°S, causing the geological transition between north and south. Trench-normal FVDs at ~140-400 km depths are widely revealed beneath the Lau Basin and Lau Ridge, indicating strong corner flows in the mantle wedge caused by slab subduction and dehydration. Compared to the northern CLSC and ELSC, the southern VFR is more influenced by the subducting Tonga slab. Trench-parallel FVDs are only observed at depths of <200 km in the subducting Tonga slab, reflecting the fossil fabric formed during the spreading stage at a mid-ocean ridge. The slab FVDs can also result from the aligned normal faults due to horizontal extension. However, trench-normal FVDs in the slab observed at greater depths may be related to extensional stress by the slab bending or some new shearing faults, reflecting a complex stress regime within the slab.

CRediT authorship contribution statement

Zhiteng Yu: Conceptualization, Formal analysis, Funding acquisition, Investigation, Methodology, Visualization, Writing – original draft. **Dapeng Zhao:** Funding acquisition, Methodology, Supervision, Writing – review & editing. **Jiabiao Li:** Funding acquisition, Supervision, Writing – review & editing.

Declaration of competing interest

The authors declare that they have no known competing financial interests or personal relationships that could have appeared to influence the work reported in this paper.

Data availability

The arrival-time data used for the anisotropic tomography were collected from the Data Management Center of Incorporated Research Institutions for Seismology (IRIS) through the IRIS Wilber 3 system (https://ds.iris.edu/wilber3/) or IRIS Web Services (https://service.iris.edu/), including the following seismic networks: the XB (1993-1995), the XT (2001-2002), the YW (2006), the YL (2009-2010), and the Z1 (2009-2010). The original earthquake catalog and arrival times at global stations were downloaded from the International Seismological Center website (http://www.isc.ac.uk/iscbulletin/search/catalogue/). The figures were plotted using the Generic Mapping Tools (https://github.com/GenericMappingTools/gmt/releases/tag/6.3.0).

Correspondence and requests for materials should be addressed to Zhiteng Yu. The obtained 3-D tomographic models are available at the Zenodo dataset repository (https://doi.org/10.5281/zenodo.7076277).

Acknowledgements

We thank the IRIS data center for providing the high-quality waveform data used in this study. Prof. Hans Thybo (the Editor), Prof. M. Gurnis and an anonymous referee provided thoughtful review comments and suggestions, which have improved this paper. This work was supported by the National Natural Science Foundation of China (41890811, JL; 41906064, ZY), the Scientific Research Fund of the Second Institute of Oceanography, MNR (JB1903, ZY), the China Postdoctoral Science Foundation (2019M652041, ZY; BX20180080, ZY), the ISblue project, Interdisciplinary graduate school for the blue planet (ANR-17-EURE-0015, ZY), the French government under the program "Investissements d'Avenir" (ZY), the Regional Council of Brittany (SAD programme) (ZY), and Japan Society for the Promotion of Science (19H01996, DZ).

Appendix A. Supplementary material

Supplementary material related to this article can be found online at https://doi.org/10.1016/j.epsl.2022.117844.

References

Alisic, L., Gurnis, M., Stadler, G., Burstedde, C., Ghattas, O., 2012. Multi-scale dynamics and rheology of mantle flow with plates. J. Geophys. Res., Solid Earth 117. https://doi.org/10.1029/2012JB009234.

Bevis, M., Taylor, F.W., Schutz, B.E., Recy, J., Isacks, B.L., Helu, S., Singh, R., Kendrick, E., Stowell, J., Taylor, B., Calmantli, S., 1995. Geodetic observations of very rapid convergence and back-arc extension at the Tonga arc. Nature 374, 249–251. https://doi.org/10.1038/374249a0.

Bonnardot, M.-A., Régnier, M., Christova, C., Ruellan, E., Tric, E., 2009. Seismological evidence for a slab detachment in the Tonga subduction zone. Tectonophysics 464, 84–99. https://doi.org/10.1016/j.tecto.2008.10.011.

Chang, S.-J., Ferreira, A.M.G., Faccenda, M., 2016. Upper- and mid-mantle interaction between the Samoan plume and the Tonga–Kermadec slabs. Nat. Commun. 7, 10799. https://doi.org/10.1038/ncomms10799.

Conder, J.A., Wiens, D.A., 2006. Seismic structure beneath the Tonga arc and Lau back-arc basin determined from joint Vp, Vp/Vs tomography. Geochem. Geophys. Geosyst. 7, Q03018. https://doi.org/10.1029/2005GC001113.

Dunn, R.A., Martinez, F., 2011. Contrasting crustal production and rapid mantle transitions beneath back-arc ridges. Nature 469, 198–202. https://doi.org/10.1038/nature09690.

Eakin, C.M., Long, M.D., Scire, A., Beck, S.L., Wagner, L.S., Zandt, G., Tavera, H., 2016. Internal deformation of the subducted Nazca slab inferred from seismic anisotropy. Nat. Geosci. 9, 56–59. https://doi.org/10.1038/ngeo2592.

Escrig, S., Bézos, A., Goldstein, S.L., Langmuir, C.H., Michael, P.J., 2009. Mantle source variations beneath the Eastern Lau Spreading Center and the nature of subduction components in the Lau basin-Tonga arc system: isotope geochemistry of Lau Basin lavas. Geochem. Geophys. Geosyst. 10, Q04014. https://doi.org/10.1029/2008GC002281.

Fischer, K.M., Parmentier, E.M., Stine, A.R., Wolf, E.R., 2000. Modeling anisotropy and plate-driven flow in the Tonga subduction zone back arc. J. Geophys. Res., Solid Earth 105, 16181–16191. https://doi.org/10.1029/1999JB900441.

Foley, B.J., Long, M.D., 2011. Upper and mid-mantle anisotropy beneath the Tonga slab. Geophys. Res. Lett. 38, L02303. https://doi.org/10.1029/2010GL046021.

Hart, S.R., Coetzee, M., Workman, R.K., Blusztajn, J., Johnson, K.T.M., Sinton, J.M., Steinberger, B., Hawkins, J.W., 2004. Genesis of the Western Samoa seamount province: age, geochemical fingerprint and tectonics. Earth Planet. Sci. Lett. 227, 37–56. https://doi.org/10.1016/j.epsl.2004.08.005.

Hawkins, J.W., 1995. The geology of the Lau Basin. In: Taylor, B. (Ed.), Backarc Basins. Springer US, Boston, MA, pp. 63–138.

Hayes, G.P., Moore, G.L., Portner, D.E., Hearne, M., Flamme, H., Furtney, M., Smoczyk, G.M., 2018. Slab2, a comprehensive subduction zone geometry model. Science 362, 58–61. https://doi.org/10.1126/science.aat4723.

Huang, Z., Tilmann, F., Comte, D., Zhao, D., 2019. *P* wave azimuthal anisotropic tomography in northern Chile: insight into deformation in the subduction zone. J. Geophys. Res., Solid Earth 124, 742–765. https://doi.org/10.1029/2018JB016389.

Jackson, M.G., Hart, S.R., Koppers, A.A.P., Staudigel, H., Konter, J., Blusztajn, J., Kurz, M., Russell, J.A., 2007. The return of subducted continental crust in Samoan lavas. Nature 448, 684–687. https://doi.org/10.1038/nature06048.

Jackson, M.G., Hart, S.R., Konter, J.G., Koppers, A.A.P., Staudigel, H., Kurz, M.D., Blusztajn, J., Sinton, J.M., 2010. Samoan hot spot track on a "hot spot highway": implications for mantle plumes and a deep Samoan mantle source. Geochem. Geophys. Geosyst. 11. https://doi.org/10.1029/2010GC003232.

Karato, S., Jung, H., Katayama, I., Skemer, P., 2008. Geodynamic significance of seismic anisotropy of the upper mantle: new insights from laboratory studies. Annu. Rev. Earth Planet. Sci. 36, 59–95. https://doi.org/10.1146/annurev.earth.36.031207.124120.

Keller, N.S., Arculus, R.J., Hermann, J., Richards, S., 2008. Submarine back-arc lava with arc signature: Fonualei Spreading Center, northeast Lau Basin, Tonga. J. Geophys. Res., Solid Earth 113. https://doi.org/10.1029/2007JB005451.

Kennett, B.L.N., Engdahl, E.R., 1991. Traveltimes for global earthquake location and phase identification. Geophys. J. Int. 105, 429–465. https://doi.org/10.1111/j.1365-246X.1991.tb06724.x.

Laske, G., Masters, G., Ma, Z., Pasyanos, M., 2013. Update on CRUST1. 0—a 1-degree global model of Earth's crust. In: Geophys. Res. Abstr., p. 2658.

Li, L., Chen, Y., Zheng, Y., Hu, H., Wu, J., 2019. Seismic evidence for plume-slab interaction by high-resolution imaging of the 410-km discontinuity under Tonga. Geophys. Res. Lett. 46, 13687–13694. https://doi.org/10.1029/2019GL084164.

Liu, X., Zhao, D., 2016. Seismic velocity azimuthal anisotropy of the Japan subduction zone: constraints from P and S wave traveltimes. J. Geophys. Res., 5086–5115. https://doi.org/10.1002/2016jb013116.

Liu, X., Zhao, D., 2017. Depth-varying azimuthal anisotropy in the Tohoku subduction channel. Earth Planet. Sci. Lett. 473, 33–43. https://doi.org/10.1016/j.epsl.2017.05.034.

Lomax, A., Virieux, J., Volant, P., Berge-Thierry, C., 2000. Probabilistic earthquake location in 3D and layered models. In: Advances in Seismic Event Location. Springer, pp. 101–134.

Lupton, J.E., Arculus, R.J., Greene, R.R., Evans, L.J., Goddard, C.I., 2009. Helium isotope variations in seafloor basalts from the Northwest Lau Backarc Basin: mapping the influence of the Samoan hotspot. Geophys. Res. Lett. 36. https://doi.org/10.1029/2009GL039468.

Martinez, F., Taylor, B., 2002. Mantle wedge control on back-arc crustal accretion. Nature 416, 417–420. https://doi.org/10.1038/416417a.

Martinez, F., Taylor, B., Baker, E.T., Resing, J.A., Walker, S.L., 2006. Opposing trends in crustal thickness and spreading rate along the back-arc Eastern Lau Spreading Center: implications for controls on ridge morphology, faulting, and hydrothermal activity. Earth Planet. Sci. Lett. 245, 655–672. https://doi.org/10.1016/j.epsl.2006.03.049.

Menke, W., Zha, Y., Webb, S.C., Blackman, D.K., 2015. Seismic anisotropy indicates ridge-parallel asthenospheric flow beneath the Eastern Lau Spreading Center. J. Geophys. Res., Solid Earth 120, 976–992. https://doi.org/10.1002/2014jb011154.

Millen, D.W., Hamburger, M.W., 1998. Seismological Evidence for Tearing of the Pacific Plate at the Northern Termination of the Tonga Subduction Zone 4.

Paige, C.C., Saunders, M.A., 1982. LSQR: an algorithm for sparse linear equations and sparse least squares. ACM Trans. Math. Softw. 8, 43–71.

Pearce, J.A., Kempton, P.D., Gill, J.B., 2007. Hf–Nd evidence for the origin and distribution of mantle domains in the SW Pacific. Earth Planet. Sci. Lett. 260, 98–114. https://doi.org/10.1016/j.epsl.2007.05.023.

Price, A.A., Jackson, M.G., Blichert-Toft, J., Hall, P.S., Sinton, J.M., Kurz, M.D., Blusztajn, J., 2014. Evidence for a broadly distributed Samoan-plume signature in the northern Lau and North Fiji Basins. Geochem. Geophys. Geosyst. 15, 986–1008. https://doi.org/10.1002/2013GC005061.

Roth, E.G., Wiens, D.A., Dorman, L.M., Hildebrand, J., Webb, S.C., 1999. Seismic attenuation tomography of the Tonga-Fiji region using phase pair methods. J. Geophys. Res., Solid Earth 104, 4795–4809. https://doi.org/10.1029/1998JB900052.

Schellart, W.P., Moresi, L., 2013. A new driving mechanism for backarc extension and backarc shortening through slab sinking induced toroidal and poloidal mantle flow: results from dynamic subduction models with an overriding plate. J. Geophys. Res., Solid Earth 118, 3221–3248. https://doi.org/10.1002/jgrb.50173.

Smith, G.P., Wiens, D.A., Fischer, K.M., Dorman, L.M., Webb, S.C., Hildebrand, J.A., 2001. A complex pattern of mantle flow in the Lau backarc. Science 292, 713–716. https://doi.org/10.1126/science.1058763.

Taylor, B., Martinez, F., 2003. Back-arc basin basalt systematics. Earth Planet. Sci. Lett. 210, 481–497. https://doi.org/10.1016/S0012-821X(03)00167-5.

Taylor, B., Zellmer, K., Martinez, F., Goodliffe, A., 1996. Sea-floor spreading in the Lau back-arc basin. Earth Planet. Sci. Lett. 144, 35–40. https://doi.org/10.1016/0012-821X(96)00148-3.

Turner, S., Hawkesworth, C., 1998. Using geochemistry to map mantle flow beneath the Lau Basin. Geology 26, 1019. https://doi.org/10.1130/0091-7613(1998)026<1019:UGTMMF>2.3.CO;2.

Wang, J., Zhao, D., 2008. P-wave anisotropic tomography beneath Northeast Japan. Phys. Earth Planet. Inter. 170, 115–133.

Wang, Z., Zhao, D., 2021. 3D anisotropic structure of the Japan subduction zone. Sci. Adv. 7, eabc9620. https://doi.org/10.1126/sciadv.abc9620.

Wang, Z., Zhao, D., Chen, X., 2022. Seismic anisotropy and intraslab hydrated faults beneath the NE Japan forearc. Geophys. Res. Lett. 49. https://doi.org/10.1029/2021GL097266.

Wei, S.S., Wiens, D.A., 2018. P-wave attenuation structure of the Lau back-arc basin and implications for mantle wedge processes. Earth Planet. Sci. Lett. 502, 187–199. https://doi.org/10.1016/j.epsl.2018.09.005.

Wei, S.S., Wiens, D.A., Zha, Y., Plank, T., Webb, S.C., Blackman, D.K., Dunn, R.A., Conder, J.A., 2015. Seismic evidence of effects of water on melt transport in the Lau back-arc mantle. Nature 518, 395–398. https://doi.org/10.1038/nature14113.

Wei, S.S., Zha, Y., Shen, W., Wiens, D.A., Conder, J.A., Webb, S.C., 2016. Upper mantle structure of the Tonga-Lau-Fiji region from Rayleigh wave tomography. Geochem. Geophys. Geosyst. 17, 4705–4724. https://doi.org/10.1002/2016GC006656.

Worthington, T.J., Hekinian, R., Stoffers, P., Kuhn, T., Hauff, F., 2006. Osbourn Trough: structure, geochemistry and implications of a mid-Cretaceous paleospreading ridge in the South Pacific. Earth Planet. Sci. Lett. 245, 685–701. https://doi.org/10.1016/j.epsl.2006.03.018.

Zha, Y., Webb, S.C., Wei, S.S., Wiens, D.A., Blackman, D.K., Menke, W., Dunn, R.A., Conder, J.A., 2014. Seismological imaging of ridge–arc interaction beneath the Eastern Lau Spreading Center from OBS ambient noise tomography. Earth Planet. Sci. Lett. 408, 194–206. https://doi.org/10.1016/j.epsl.2014.10.019.

Zhao, D., Hasegawa, A., Horiuchi, S., 1992. Tomographic imaging of P and S wave velocity structure beneath northeastern Japan. J. Geophys. Res. 97, 19909–19928. https://doi.org/10.1029/92jb00603.

Zhao, D., Xu, Y., Wiens, D.A., Dorman, L., Hildebrand, J., Webb, S., 1997. Depth extent of the Lau back-arc spreading center and its relation to subduction processes. Science 278, 254–257. https://doi.org/10.1126/science.278.5336.254.

Zhao, D., Yanada, T., Hasegawa, A., Umino, N., Wei, W., 2012. Imaging the subducting slabs and mantle upwelling under the Japan Islands. Geophys. J. Int. 190, 816–828. https://doi.org/10.1111/j.1365-246X.2012.05550.x.

Zhao, D., Yu, S., Liu, X., 2016. Seismic anisotropy tomography: new insight into subduction dynamics. Gondwana Res. 33, 24–43. https://doi.org/10.1016/j.gr.2015.05.008.

Zhou, Z., Lin, J., Behn, M.D., Olive, J.-A., 2015. Mechanism for normal faulting in the subducting plate at the Mariana Trench. Geophys. Res. Lett. 42, 4309–4317. https://doi.org/10.1002/2015GL063917.